Microscopic description of fusion hindrance in symmetric Ni+Ni and asymmetric $^{12}C + ^{198}Pt$ systems

M. Rashdan

Department of Mathematics and Theoretical Physics, NRC Atomic Energy Authority, Cairo, Egypt

(Received 7 February 2020; accepted 9 October 2020; published 6 November 2020)

Hindrance at deep subbarrier energies for the symmetric $^{58}Ni + ^{58}Ni$, $^{64}Ni + ^{64}Ni$, and asymmetric $^{12}C + ^{198}Pt$ systems is investigated using microscopic energy and the density-dependent G-matrix effective interaction. The proton and neutron density distributions of target and projectile are derived from Skyrme-Hartree-Fock calculations. A fair agreement with the data of the fusion excitation functions and astrophysical S factors have been obtained without any fitting parameters. Hindrance is naturally reproduced at deep subbarrier energies, which is consistent with experimental observations.

DOI: 10.1103/PhysRevC.102.055804

I. INTRODUCTION

A steep falloff in fusion cross section between heavy ions has been observed, recently, for several systems at deep subbarrier energies and has been identified as a fusion hindrance [1–6]. The phenomenon of a hindrance has often been analyzed in terms of the S factor, where a maximum in $S(E)$ appears at the threshold energy of observing fusion hindrance [3], or by the logarithmic derivative of the fusion cross section [4]. Several phenomenological potentials have been introduced to describe the hindrance phenomenon. For example, Misicu and Esbensen [7] proposed a potential with a shallow pocket and a repulsive core to describe fusion reactions at subbarrier energies. Although the repulsive core could modify the depth and the shape of the minima of the internuclear potential, the distance at which the repulsive core is added has been taken as a free parameter. Furthermore, the assumption that the fusion cross section can be described by two different potentials seems to be inadequate. Ichikawa [8] investigated fusion hindrance in reactions of $^{58,60}Ni$ colliding with Ni and other nuclei using Yukawa-plus exponential (YPE) potential. The YPE model would describe fusion hindrance but it has seven free input parameters that have been adjusted for each interacting pairs to fit the data.

Recently, Hagino *et al.* [9] investigated the relationship between the maximum of the astrophysical S factor and the hindrance phenomenon in heavy-ion fusion reactions at deep subbarrier energies by using two Woods-Saxon (WS) potentials. They found that the astrophysical S factor could provide a convenient tool to analyze the deep subbarrier hindrance phenomenon, even though the S factor may have a strong energy dependence for heavy-ion systems. However, the two WS potentials used by Hagino *et al.* have six free parameters which were fit for each colliding pairs to reproduce the data.

The aim of the present work is to investigate fusion hindrance within a microscopic parameter-free internuclear potential, which depends on the incident energy as well as the nuclear densities of the interacting nuclei. This internuclear potential is derived from Brueckner G matrix, which is the solution of the Bethe-Goldstone equation [10–12]. The nuclear densities are input in this approach and are derived microscopically from Skyrme-Hartree-Fock (SHF) calculations, adopting SKRA interaction, which well describe finite nuclei [13]. The derived potential will be used to calculate the fusion excitation function and the astrophysical S factors for the systems $^{58}Ni + ^{58}Ni$, $^{64}Ni + ^{64}Ni$, and $^{12}C + ^{198}Pt$. Calculations are presented in Sec II. Results are presented and discussed in Sec. III. Section IV presents the summary and conclusion.

II. CALCULATIONS

The interaction potential between two colliding nuclei separated by a distance R can be written as [10–12]

$$V(R; K_r) = \int d^3r[H(\mathbf{r}, R; K_r) - H(\mathbf{r}, \infty; K_r)], \quad (1)$$

where K_r is the relative momentum per nucleon, which depends on the incident energy of the projectile; $K_r = (\frac{2m}{\hbar^2}\frac{E_{\rm lab}}{A_P})^{1/2}$. The energy density functional H is written as

$$H(\mathbf{r}, R; Kr) = \tau(\rho_P, \rho_T; Kr) + \Pi(\rho_P, \rho_T; Kr) + H_{\rm cor}(\rho_p, \rho_n), \quad (2)$$

where ρ_P and ρ_T are the projectile and target densities. The first term in Eq. (2) is the kinetic-energy density which is calculated in momentum space, from

$$\tau(\rho_P, \rho_T; Kr) = \frac{\hbar^2}{2m}\left[g\int_F \frac{d^3k}{(2\pi)^3}(k - K_G)^2 + K_G^2\rho\right], \quad (3)$$

where g is a spin-isospin degeneracy factor and K_G is a reference center-of-mass (c.m.) momentum ($K_G = \frac{\rho_P}{\rho}K_r$, where ρ is the total density of the system). $\int_F$ stands for the integration over the occupied states for two colliding nuclear matters.

The second term is the potential-energy density functional $\Pi(\rho_P, \rho_T; Kr)$, which is calculated, in momentum space, from the reaction matrix G, which is the solution of the Bethe-Goldstone equation,

$$G = V + V\frac{Q}{W - H_0 + i\epsilon}G. \quad (4)$$

where H_0 is the single-particle Hamiltonian and Q is the Pauli operator blocks occupied states in the core. V is a microscopic bare nucleon-nucleon interaction taken to be the Reid soft-core potential. The potential-energy density $\Pi(\rho_P, \rho_T; Kr)$ is calculated from the G matrix,

$$\Pi(\rho_P, \rho_T; Kr) = \frac{1}{2}\sum_{\text{spin}}\sum_{\text{isospin}}\int_F \frac{d^3k}{(2\pi)^3}\int_F \frac{d^3k'}{(2\pi)^3}\langle kk' \mid G \mid kk'\rangle_a, \quad (5)$$

where the subscript a indicates antisymmetrization of the matrix element. Equations (3)–(5) are calculated in momentum-space configuration of two colliding nuclear matters (two Fermi spheres), using the generalized local density approximation. In this approximation, at each separation distance R, one can relate two Fermi radii, k_{F_P} and k_{F_T}, by the densities of the interaction nuclei $\rho_{\rm P}$ $(=\frac{2}{3\pi^2}k_{F_P}^3)$ and $\rho_{\rm T}$ $(=\frac{2}{3\pi^2}k_{F_T}^3)$, which yields two Fermi spheres whose centers are separated in momentum space by the relative momentum per nucleon Kr, since each projectile nucleon has an average momentum Kr. When the two Fermi spheres overlap a region of double occupancy is obtained which is forbidden by the Pauli principle. Therefore, the momentum distribution has to be changed to avoid the region of double occupancy. In this case, the two Fermi spheres are enlarged but keep the same overall density. To this end, one defines two new Fermi radii k'_{F_P} and k'_{F_T}, which are determined from the old ones using volume conservation. The new radii are of course larger than the old ones due to the Pauli principle and they have to be calculated numerically using an iterative procedure (see Ref. [10] for details).

The last term in Eq. (2) is a correction term due to surface and symmetry energy corrections [11,12]. The proton and neutron densities of the combined system are given by the sum of target and projectile densities, i.e.,

$$\rho_{\rm p,n} = \rho^T_{\rm p,n}(\mathbf{r}) + \rho^P_{\rm p,n}|r - R|. \quad (6)$$

These densities are calculated from Skyrme-Hartree-Fock calculations by using the Skyrme interaction SKRA [13]. Other Skyrme interactions are also used for comparison.

III. RESULTS AND DISCUSSION

The total densities of ^{58}Ni and ^{64}Ni are displayed in Fig. 1. As shown from this figure, a neutron skin is formed for ^{64}Ni due to the larger number of neutrons. This skin is expected to increase the nuclear potential and fusion cross section. The nuclear and total (nuclear + Coulomb) potentials of ^{58}Ni + ^{58}Ni and ^{64}Ni + ^{64}Ni calculated in the present G-matrix approach at the energy around the Coulomb barrier, 5 MeV/u, using SHF densities, adopting the SKRA interaction, are displayed in Fig. 2. As shown from this figure the

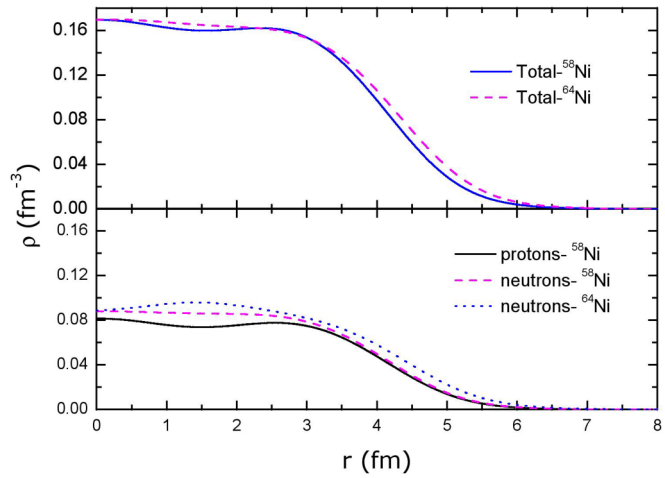

FIG. 1. The SHF densities of ^{58}Ni and ^{64}Ni calculated adopting SKRA interaction.

nuclear potential of ^{64}Ni + ^{64}Ni is deeper than the potential of ^{58}Ni + ^{58}Ni in the surface and tail region due to the increases in the nuclear densities of ^{64}Ni in these regions, as shown from Fig. 1. This deeper potential decreases the fusion barrier as shown from Fig. 2. Figure 3 shows the energy dependence of the nuclear and total potentials of ^{64}Ni + ^{64}Ni. As shown from this figure the potential is shallow at zero energy and becomes deeper with increasing energy due to the decreasing in Pauli blocking effects. As a result, the interaction barrier decreases and shifts outwards with increasing energy, which is expected to increase the probability of fusion. The barrier height decreases by about 2 MeV with increasing energy from zero laboratory energy to 5 MeV/u, i.e., around the Coulomb barrier. On the other hand, the depth of the potential pocket increases by about 8 MeV, as shown from Fig. 3. This dramatic energy dependence of the nuclear potential is interesting, where it is expected to strongly affect the fusion

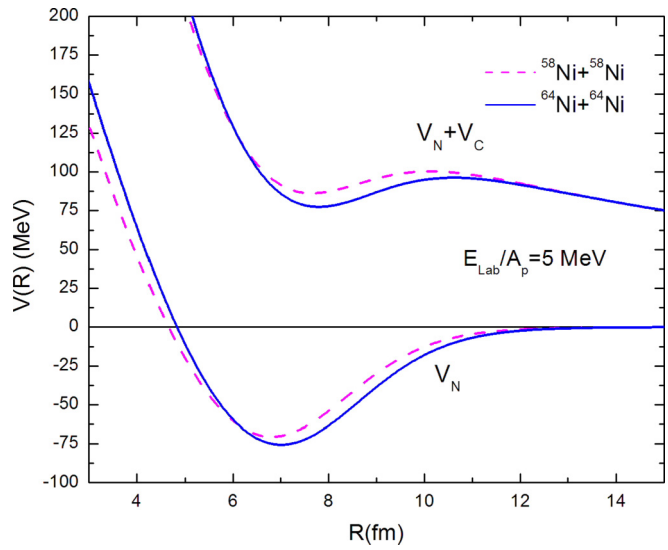

FIG. 2. The nuclear and total (nuclear + Coulomb) potentials of ^{58}Ni + ^{58}Ni and ^{64}Ni + ^{64}Ni calculated at 5 MeV/u.

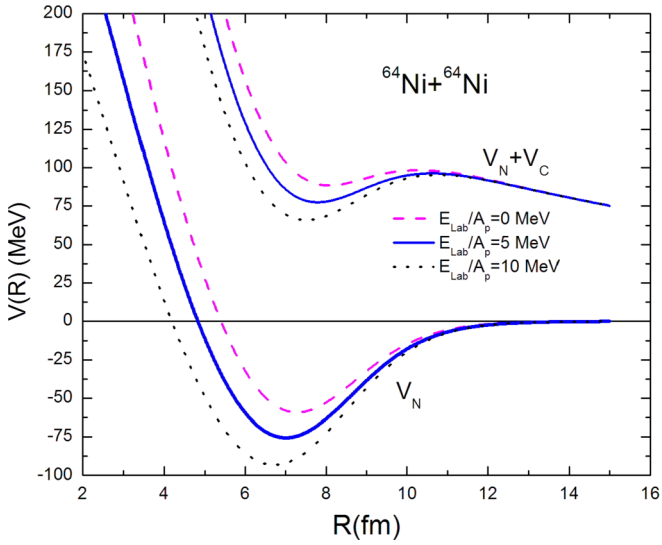

FIG. 3. The energy dependence of the nuclear and total potentials of $^{64}\mathrm{Ni}+{}^{64}\mathrm{Ni}$.

cross section at subbarrier energies, which is very important for the investigation of hindrance phenomena.

The calculated internuclear potentials are used to calculate the fusion cross sections using the CCFULL code [14]. However, in the CCFULL code the input potential is in a WS form. Thus, the calculated *G*-matrix potentials are fit to a WS form. Figure 4 shows the WS potential fit to the *G*-matrix potential for the system $^{58}\mathrm{Ni}+{}^{58}\mathrm{Ni}$ at energy 5 MeV/u. Figures 5(a)–5(c) show the energy dependence of the WS parameters, which are fit to the potentials calculated from the *G*-matrix effective interaction at different energies. As shown from this figure the depth, V_0 increases with increasing energy. The diffuseness a slightly increases and the radius R_0 slightly decreases with increasing energy. The ex-

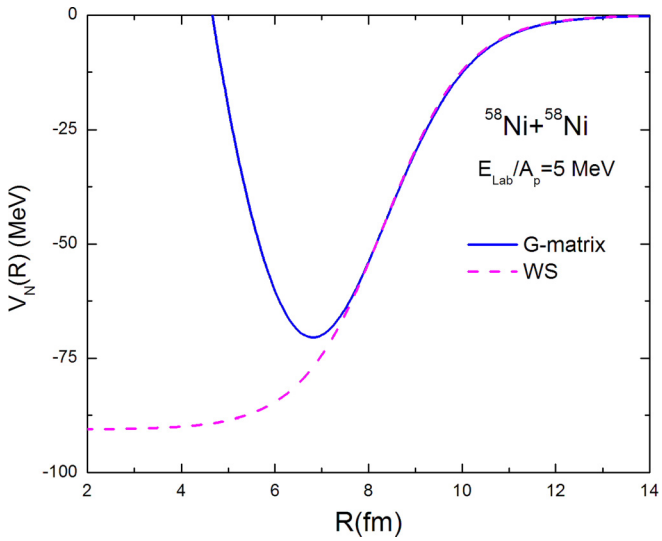

FIG. 4. The WS potential fit to the *G*-matrix potential at $E_{\mathrm{lab}}/A_p = 5$ MeV. The WS parameters are found to be $V_0 = 90.554$ MeV, $r_0 = 1.0784$ fm, and $a = 0.8856$ fm.

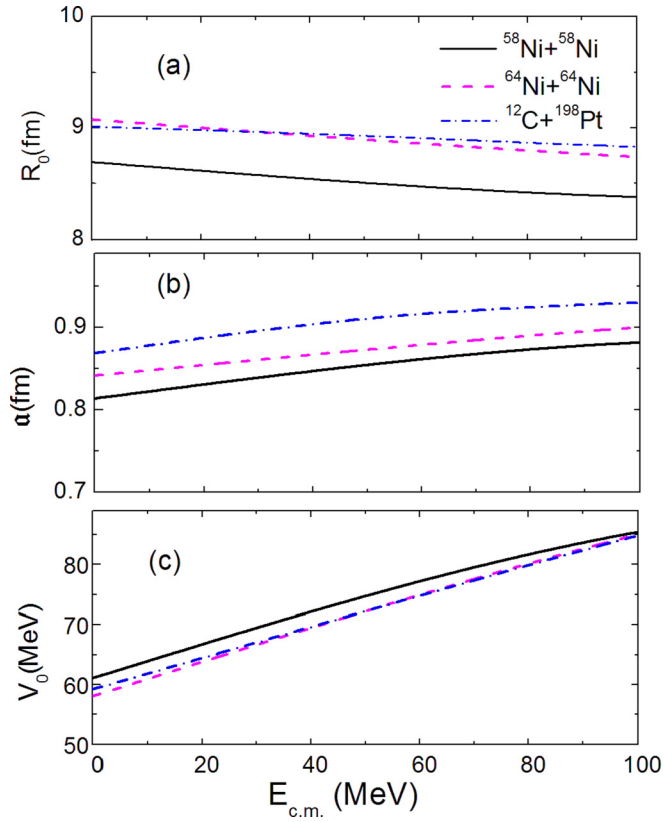

FIG. 5. The energy dependence of the WS potential parameters R_0, a, and V_0 shown in panels (a)–(c), respectively, fit to the interaction potential calculated from Brueckner *G* matrix at different energies.

citation functions of the symmetric systems $^{58}\mathrm{Ni}+{}^{58}\mathrm{Ni}$, and $^{64}\mathrm{Ni}+{}^{64}\mathrm{Ni}$ and the asymmetric system $^{12}\mathrm{C}+{}^{198}\mathrm{Pt}$ calculated using the energy dependence potentials with and without considering the coupling to inelastic excited states are shown in Figs. 6–9. The input parameters for the coupling strengths in the coupled-channels (CC) calculations are listed in Table I. For the symmetric Ni + Ni systems, the experimental data are taken from Beckerman *et al.* [1] and Jiang *et al.* [2], while for the asymmetric $^{12}\mathrm{C}+{}^{198}\mathrm{Pt}$ system they are taken from Shrivastava *et al.* [15]. As shown from these figures the fusion excitation functions are fairly reproduced by the present *G*-matrix energy-dependent internuclear potentials. The steep falloff observed in the fusion cross sections at very low subbarrier energies are very well reproduced. For the newly observed fusion asymmetric system $^{12}\mathrm{C}+{}^{198}\mathrm{Pt}$, the experimental fusion cross section is also automatically reproduced at deep subbarrier energies by the present microscopic potential without any need to phenomenological adjustable parameters or damping factors of coupled-channels effect, as done in the calculations of Refs. [8,9,15,16]. This is because the present microscopic internuclear potential is more shallow at very low energies and becomes deeper with increasing energy. This shallow potential reduces the cross section at deep subbarrier energies in agreement with the data. If I use the potential calculated at the energy around the Coulomb barrier, at $E_{\mathrm{lab}}/A_P = 5$ MeV/u, an increase in

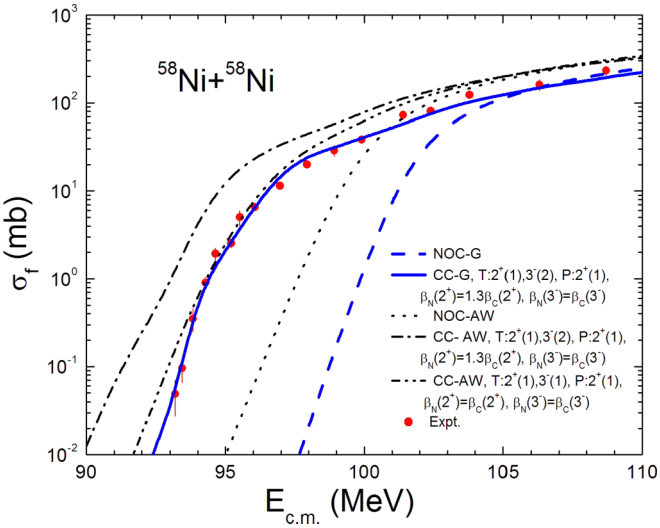

FIG. 6. The excitation functions of ^{58}Ni + ^{58}Ni. The dashed, NOC (no coupling), and solid, CC, lines represent calculations using *G*-matrix energy-dependent potentials with SHF densities, adopting SKRA interactions. The surface excitation parameters used in the coupled channels calculations are listed in Table I. The numbers in brackets denote the number of phonons. Calculations using AW potential are denoted by dotted and dash-dotted lines. The dash-double dotted line is calculated with the AW potential but using one-phonon excitations and equal Coulomb and nuclear deformations. The experimental data are taken from Beckerman *et al.* [1].

the cross section is obtained, especially at lower energies in disagreement with the data, as shown from Fig. 7. On the other hand, if I use the potential calculated at zero energy, a reduction in the cross section below the barrier is obtained, in disagreement with the data, as shown from Fig. 7. This is due to the shallow potential at zero energy. Indeed, it has

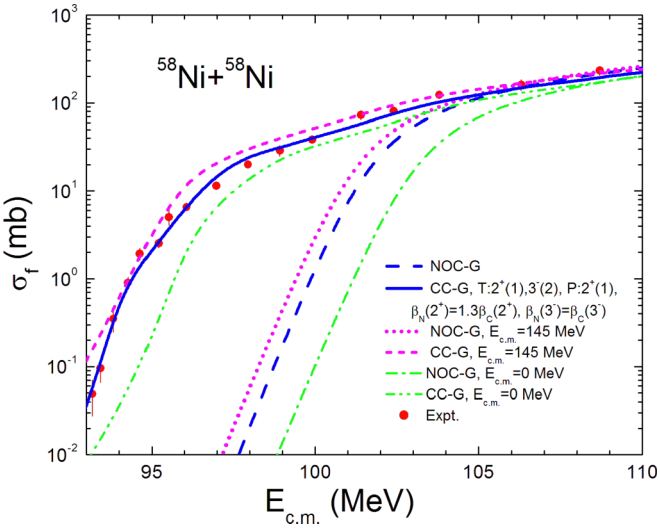

FIG. 7. The excitation functions of ^{58}Ni + ^{58}Ni calculated using the *G*-matrix energy-dependent potentials (dashed and solid lines) compared with that calculated using *G*-matrix potentials calculated at zero and $E_{\rm lab}/A_p = 5$ MeV ($E_{\rm c.m.} = 145$ MeV).

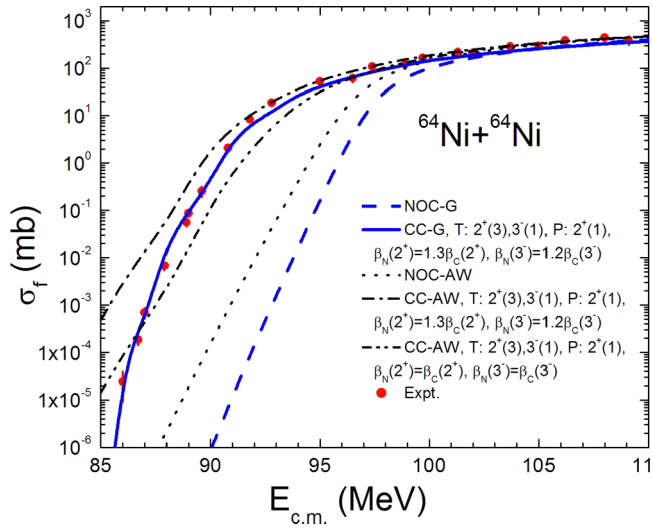

FIG. 8. Same as Fig. 6 but for ^{64}Ni + ^{64}Ni. The experimental data are taken from Jiang *et al.* [2].

been pointed out in Ref. [7] that energy density approaches produce shallow potentials, but they lead to excessively high potential barriers, underestimating the fusion cross section at near-barrier energies. However, by using an energy-dependent potential calculated in the energy density approach, the potential is modified, leading to a decreasing barrier with increasing energy, as indicated in Fig. 3. This is obviously due to the increases in the attractive nuclear potential which, finally, leads to well-reproduced fusion cross sections at all energies, as shown from Figs. 6–9 without the need for any changes in the parameters of the calculation.

It is worth mentioning that the Coulomb deformation parameters adopted in the CC calculations, given Table I, are taken from experiments, and they were listed in Ref. [16]. The

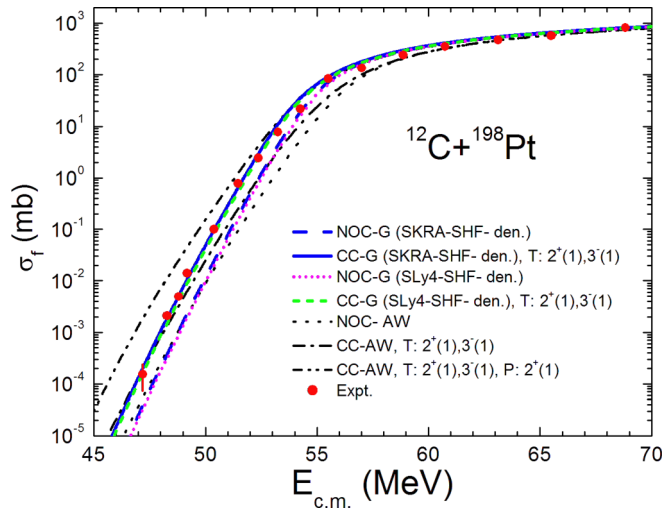

FIG. 9. Same as Fig. 6 but for ^{12}C + ^{198}Pt. The short-dotted and short-dashed lines represent calculations using *G*-matrix energy-dependent potentials but with the SLy4 interaction for SHF densities. The experimental data are taken from Shrivastava *et al.* [15].

TABLE I. Input parameters for the coupling strengths in the CC calculations. λ^π refers to the multipolarity and the parity of a state of excitation energy E_x. The Coulomb and nuclear deformation parameters are denoted by β_C and β_N, respectively. The last column is the number of phonons, N_{ph}, included in the calculations. The data for excitation energies and Coulomb deformations are taken from Ref. [16] and references therein.

System	λ^π	E_x (MeV)	β_C	β_N	N_{ph}
^{58}Ni + ^{58}Ni, T:	2^+	1.45	0.187	0.243	1
	3^-	4.47	0.2	0.2	2
P:	2^+	1.45	0.187	0.243	1
^{64}Ni + ^{64}Ni, T:	2^+	1.346	0.193	0.25	3
	3^-	3.56	0.165	0.198	1
P:	2^+	1.346	0.193	0.25	1
^{12}C + ^{198}Pt, T:	2^+	0.407	0.11	0.11	1
	3^-	1.5	0.1	0.1	1

nuclear deformations cannot be determined from experiments and they are almost taken differently from the Coulomb deformation. In Ref. [16] for ^{58}Ni + ^{58}Ni reaction, β_N of ^{58}Ni was increased to $1.21\beta_C$ for the 2^+ and $\beta_N = \beta_C$ for 3^- excited states. I follow a similar prescription for the same reaction, where β_N is increased to $1.3\beta_C$ for the 2^+ and $\beta_N = \beta_C$ for 3^- excited states. For the ^{64}Ni + ^{64}Ni reaction, the nuclear deformation of ^{64}Ni was taken from Ref. [16] is larger than the Coulomb deformation for both 2^+ and 3^- excited states. In the present work, the values $\beta_N = 1.3\beta_C$ for the 2^+ and $\beta_N = 1.2\beta_C$ for the 3^- excited states of ^{64}Ni are considered. These values are larger than that considered in Ref. [16] but are consistent with other previous work [12] in which β_N was increased to $1.4\beta_C$ for ^{64}Ni. For the C + Pt reaction, the nuclear and Coulomb deformations are taken equally as considered in Ref. [16].

It is important to make comparisons with the results of CC calculations with some standard nuclear interactions, like the Akyüz-Winther (AW) potential [17], which has the practical advantage of being parametrized by WS functions, which is appropriate for the use of the CCFULL code. In Figs. 6, 8, and 9, calculation of the excitation functions using the AW potential with and without coupling to inelastic excitations are presented. As shown from these figures, the AW potential fails to reproduce the cross sections below the barrier, whereas it overestimates the data at lower energies, as expected.

It is also important to make comparisons with different Skyrme interactions used in SHF calculations for generating the nuclear densities, which are inputs in the *G*-matrix potential. Figure 9 shows the excitation function for the ^{12}C + ^{198}Pt system calculated using the Skyrme interaction SLy4 [18] in the SHF calculations for the nuclear densities in a comparison with the SKRA interaction. As shown from this figure, the two Skyrme interactions give similar good results, since both well describe the nuclear densities and, consequently, the nuclear potential and fusion cross sections. The Skyrme interaction SkM* [19] is also tested and is found to also give similar results. This shows that the sensitivity to Skyrme interactions that well describe the nuclear densities are weak, which, on the other hand, favors the generality of the present approach in calculating the internuclear potential and fusion cross section.

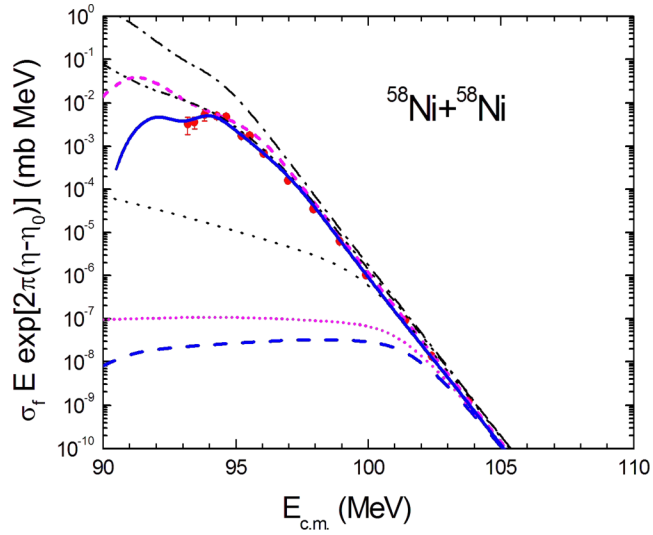

FIG. 10. Same as Fig. 6 but for the astrophysical *S* factors. Calculations using *G*-matrix potentials but calculated at fixed energy $E_{\text{c.m.}} = 145$ MeV are shown by short-dotted and short-dashed lines.

The astrophysical *S* factor is a powerful tool for studying fusion hindrance. The corresponding *S* factors of the fusion reactions of Figs. 6, 8, and 9 are shown in Figs. 10–12. As shown from these figures, a maximum in the *S* factor is predicted by the present energy-dependent internuclear potential at the corresponding subthreshold energy of hindrance, which is consistent with the observed experimental data. The agreement in the *S* factor is better than that obtained in Ref. [9], which used two different phenomenological Woods-Saxon potentials, with six adjustable parameters, where the first and second WS potentials were fit for two different energy regions of the fusion cross section, which were taken *ad hoc*. In Ref. [16], many phenomenological potentials such as

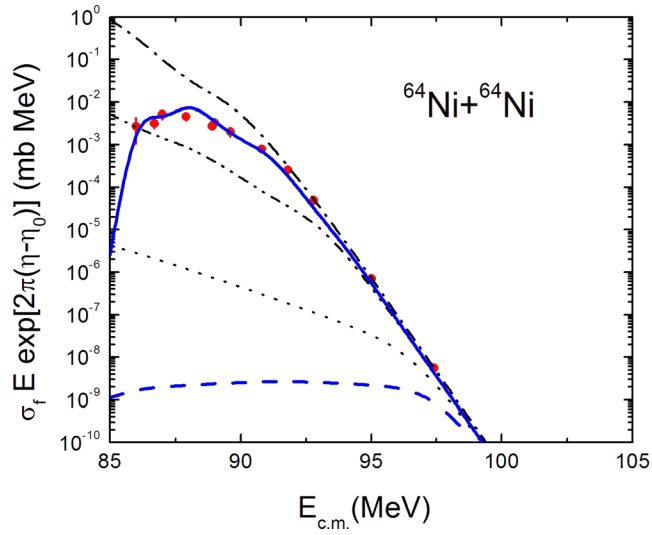

FIG. 11. Same as Fig. 8 but for the astrophysical *S* factors.

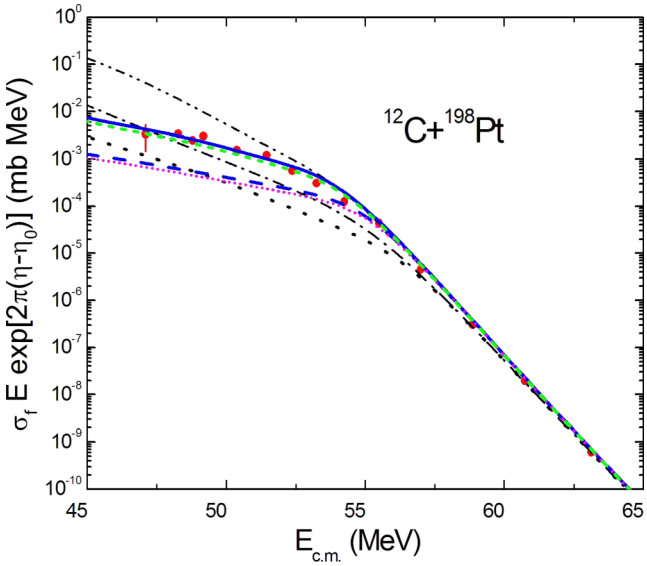

FIG. 12. Same as Fig. 9 but for the astrophysical *S* factors.

Krappe-Nix-Sierk [20], Bass (1980) [21], and AW were used to describe the fusion cross section with a phenomenological damping factor to describe fusion hindrance. In the present microscopic approach, the fusion cross sections at subbarrier and deep subbarrier energy as well as the corresponding *S* factors, where a maximum occurs at hindrance deep subbarrier energy, are satisfactorily reproduced with single-channel microscopic energy and density-dependent internuclear potential, without any fitting or damping parameters. This is an important attempt for describing fusion hindrance through a microscopic parameter-free approach, which depends on the incident energy and the density distributions of the interacting nuclei.

IV. CONCLUSION

Calculations of the fusion excitation functions and the astrophysical *S* factors based on a microscopic parameter-free energy and density-dependent internuclear potential are presented to investigate hindrance phenomena in heavy-ion reactions at subbarrier energies. The internuclear potential is derived by solving the Bethe-Goldstone equation, locally, in momentum-space configuration of two colliding nuclear matters, starting from the realistic Reid-soft core potential. The nuclear densities are derived from SHF calculations. The model is a microscopic parameter-free approach. The fusion excitation functions and the *S* factors are well described where a good agreement with the experimental data is obtained. Hindrance is satisfactorily reproduced, without any adjustable parameter or damping factors, due to the energy and density dependence of the internuclear potential.

[1] M. Beckerman *et al.*, Phys. Rev. Lett. **45**, 1472 (1980); M. Beckerman, J. Ball, H. Enge, M. Salomaa, A. Sperduto, S. Gazes, A. DiRienzo, and J. D. Molitoris, Phys. Rev. C **23**, 1581 (1981).
[2] C. L. Jiang *et al.*, Phys. Rev. Lett. **89**, 052701 (2002).
[3] C. L. Jiang, H. Esbensen, B. B. Back, R. V. F. Janssens, and K. E. Rehm, Phys. Rev. C **69**, 014604 (2004); B. B. Back, H. Esbensen, C. L. Jiang, and K. E. Rehm, Rev. Mod. Phys. **86**, 317 (2014).
[4] K. Hagino, N. Rowley, and M. Dasgupta, Phys. Rev. C **67**, 054603 (2003).
[5] G. Montagnoli *et al.*, Phys. Rev. C **82**, 064609 (2010); Nucl. Phys. A **834**, 159c (2010); Phys. Rev. C **85**, 024607 (2012); Phys. Rev. C **87**, 014611 (2013).
[6] G. Montagnoli *et al.*, Phys. Rev. C **97**, 024610 (2018); J. Khuyagbaatar *et al.*, *ibid.* **97**, 064618 (2018).
[7] S. Misicu and H. Esbensen, Phys. Rev. Lett. **96**, 112701 (2006); Phys. Rev. C **75**, 034606 (2007).
[8] T. Ichikawa, Phys. Rev. C **92**, 064604 (2015).
[9] K. Hagino, A. B. Balantekin, N. W. Lwin, and Ei Shwe Zin Thein, Phys. Rev. C **97**, 034623 (2018).
[10] M. Trefz, A. Faessler, and W. H. Dickhoff, Nucl. Phys. A **443**, 499 (1985).
[11] M. Rashdan, Phys. Rev. C **88**, 024615 (2013); **91**, 054613 (2015); Eur. Phys. J. A **56**, 130 (2020).
[12] M. Rashdan, Eur. Phys. J. A **50**, 96 (2014).
[13] M. Rashdan, Mod. Phys. Lett. A **15**, 1287 (2000).
[14] K. Hagino, N. Rowley, and A. T. Kruppa, Comput. Phys. Commun. **123**, 143 (1999).
[15] A. Shrivastava *et al.*, Phys. Lett. B **755**, 332 (2016).
[16] K. Cheng and C. Xu, Nucl. Phys. A **992**, 121642 (2019).
[17] A. Winther, Nucl. Phys. A **594**, 203 (1995); T. Ichikawa, K. Hagino, and A. Iwamoto, Phys. Rev. C **75**, 064612 (2007).
[18] E. Chabanat, P. Bonche, P. Haensel, J. Meyer, and R. Schaeffer, Nucl. Phys. A **635**, 231 (1998).
[19] J. Bartel, P. Quentin, M. Brack, C. Guet, and H.-B. Hakansson, Nucl. Phys. A **386**, 79 (1982).
[20] H. J. Krappe, J. R. Nix, and A. J. Sierk, Phys. Rev. C **20**, 992 (1979).
[21] R. Bass, *Nuclear Reactions with Heavy Ions* (Springer-Verlag, New York, 1980).